Available online at www.sciencedirect.com
SCIENCE DIRECT®
Journal of Computational Physics 213 (2006) 844–861
JOURNAL OF COMPUTATIONAL PHYSICS
www.elsevier.com/locate/jcp

A multi-phase SPH method for macroscopic and mesoscopic flows

X.Y. Hu [a,b,*], N.A. Adams [b]

[a] Institut für Strömungsmechanik, Technische Universität Dresden, 01062 Dresden, Germany
[b] Lehrstuhl für Aerodynamik, Technische Universität München, 85748 Garching, Germany

Received 4 April 2005; received in revised form 8 July 2005; accepted 2 September 2005
Available online 18 October 2005

Abstract

A multi-phase smoothed particle hydrodynamics (SPH) method for both macroscopic and mesoscopic flows is proposed. Since the particle-averaged spatial derivative approximations are derived from a particle smoothing function in which the neighboring particles only contribute to the specific volume, while maintaining mass conservation, the new method handles density discontinuities across phase interfaces naturally. Accordingly, several aspects of multi-phase interactions are addressed. First, the newly formulated viscous terms allow for a discontinuous viscosity and ensure continuity of velocity and shear stress across the phase interface. Based on this formulation thermal fluctuations are introduced in a straightforward way. Second, a new simple algorithm capable for three or more immiscible phases is developed. Mesocopic interface slippage is included based on the apparent slip assumption which ensures continuity at the phase interface. To show the validity of the present method numerical examples on capillary waves, three-phase interactions, drop deformation in a shear flow, and mesoscopic channel flows are considered.

Keywords: Multi-phase flows; Macroscopic and mesoscopic flows; Particle method

1. Introduction

For decreasing length scales and increasing time scales, multi-phase forces, such as those caused by viscosity difference or surface tension, may become comparable to inertial forces even though the overall flow can be considered as macroscopic. When length scales decrease further to the order of μm or smaller the flow may become mesoscopic. In a mesoscopic flow multi-phase forces usually dominate inertial forces, and thermal fluctuations affect the flow behavior strongly. Many industrial, environmental, and biological applications involve macroscopic and mesoscopic flow problems with the presence of multiple fluid phases. A variety of methods has been developed to study the above problems numerically. In general, there are two main approaches which can be distinguished by the way of handling phase interfaces: one is the Eulerian approach,

* Corresponding author. Tel.: +49 89 289 16152; fax: +49 89 289 16139.
E-mail address: xiangyu.hu@aer.mw.tum.de (X.Y. Hu).

0021-9991/$ - see front matter © 2005 Elsevier Inc. All rights reserved.
doi:10.1016/j.jcp.2005.09.001

such as the volume of fluid (VOF) method [36], the level set method [39] and the lattice Boltzmann method (LBM) [2]; the other is the Lagrangian approach, such as vortex methods [6,22], molecular dynamics (MD) [21], and dissipative particle dynamics (DPD) [18].

The smoothed particle hydrodynamics (SPH) method is a fully Lagrangian, grid free method in which a smoothing kernel is introduced to approximate functions and their spatial derivatives originating from the interactions carried by neighboring particles. The SPH algorithm itself is similar to that of MD but uses additional thermodynamic variables which are obtained by a coarse graining procedure from the underlying microscopic (molecular) physics. Since its introduction by Lucy [25] and Gingold and Monaghan [12], SPH has been applied to a wide range of macroscopic flow problems [26]. Recently, the method has been extended to smoothed dissipative particle dynamics (SDPD) for mesoscopic problems [9]. Unlike DPD [8,16], SDPD allows to choose an equation of state and to specify transport coefficients directly. Thermal fluctuations can also be included in a physically consistent way, by which the fluctuation magnitude increases naturally while the physical scale of the problem decreases to the mesoscopic scale.

Despite its fully Lagrangian property, when the standard formulation of SPH is applied to multi-phase flows only small density differences are permitted between the considered phases because it is implicitly assumed that the density gradient is much smaller than that of the smoothing kernel [27,28]. As a remedy, Richie and Thomas [35] suggest a summation of the particle-averaged pressure, not density, to handle large density gradients. However, their method does not satisfy mass conservation. Colagrossi and Landrini [5] modify the approximation form of spatial derivatives to diminish the effects of large density difference across the interface. However, since the density summation is replaced by a non-conservative density evolution equation mass conservation is not satisfied either. Although the conservation errors are decreased somewhat by a special density re-initialization approach, they may accumulate and affect the flow behavior considerably in long time computations.

In this paper, the basic approximations for particle-averaged spatial derivatives are derived from a particle smoothing function in which neighboring particles only contribute to the specific volume but not to the density. The resulting algorithm resolves a density discontinuity at a phase interface naturally and satisfies mass conservation since a density summation equation is employed. With the new algorithm several aspects of multi-phase interactions are addressed. First, newly formulated viscous terms allow for a viscosity discontinuity and ensure continuity of velocity and shear stress across the phase interface. Based on this formulation mesoscopic thermal fluctuations are introduced in a straightforward way. Second, a new algorithm capable of handling three or more immiscible phases is developed. It is simple and conservative, and circumvents the difficulties of calculating the normalized interface direction and curvature near the fringe of the interface. Furthermore, mesoscopic interface slippage is modeled based on the apparent-slip assumption which ensures continuity at the phase interface. In this paper, the isothermal form of the Navier–Stokes equations is considered. The extension of the method to include a transport equation for energy is straightforward.

2. Method

We consider the isothermal Navier–Stokes equations on a moving Lagrangian grid

$$\frac{\mathrm{d}\rho}{\mathrm{d}t} = -\rho\nabla\cdot\mathbf{v}, \tag{1}$$

$$\frac{\mathrm{d}\mathbf{v}}{\mathrm{d}t} = \mathbf{g} - \frac{1}{\rho}\nabla p + \mathbf{F} + \frac{\mathbf{F}^{(1)}}{\rho}, \tag{2}$$

where ρ, $\mathbf{v}$ and $\mathbf{g}$ are material density, velocity and body force, respectively. A simple equation of state is $p = -\kappa_{\mathrm{T}}V$ in which κ_{T} is the isothermal compressibility. It can be rewritten as

$$p = a^2\rho. \tag{3}$$

When Eqs. (1) and (2) are used for modeling of low Reynolds number incompressible flows with the artificial-compressibility method a is equal to the artificial speed of sound. An alternative equation of state for incompressible flows is

$$p = p_0\left(\frac{\rho}{\rho_0}\right)^{\gamma} + b, \tag{4}$$

where p_0, ρ_0, γ and a are parameters. The parameters in Eqs. (3) and (4) may be chosen based on a scale analysis [26,29,30] so that the density variation is less than a given value. $\mathbf{F}$ denotes the viscous force

$$\mathbf{F} = \frac{1}{\rho}\nabla\cdot\Pi^{(v)}, \tag{5}$$

where the shear stress is $\Pi^{(v)} = \eta(\nabla\mathbf{v} + \nabla\mathbf{v}^{\mathrm{T}})$ if the bulk viscosity is assumed as $\zeta = (2/d)\eta$, and d is the spatial dimension. For incompressible flow the viscous force simplifies to

$$\mathbf{F} = \nu\nabla^2\mathbf{v}, \tag{6}$$

where $\nu = \eta/\rho$ is the kinematic viscosity. $\mathbf{F}^{(1)}$ denotes the surface force which acts at the interface only. For an immiscible mixture the surface force is given as

$$\mathbf{F}^{(1)} = \alpha(\nabla\cdot\hat{\mathbf{n}})\hat{\mathbf{n}}, \tag{7}$$

where α is surface-tension coefficient, $\kappa = \nabla\cdot\hat{\mathbf{n}}$ and $\hat{\mathbf{n}}$ are curvature and normalized interface direction, respectively. Note that body force, pressure, and surface force are conservative forces. Since diffusion effects are neglected in the current model dissipative effects are due to viscous forces only.

2.1. Smoothed particle in a multi-phase mixture

For an S-phase mixture we introduce the smoothing function for particle i

$$\chi_i(\mathbf{r}) = \frac{W(\mathbf{r}-\mathbf{r}_i,h)}{\sum_k W(\mathbf{r}-\mathbf{r}_k)} = \frac{W_i(\mathbf{r})}{\sigma(\mathbf{r})}, \tag{8}$$

where $\mathbf{r}_i$ gives the position of particle i, $k = 1,\ldots,N$, N is the total particle number and h is the smoothing length. $W(\mathbf{r})$ is a generic shape function known as the SPH smoothing kernel which is radially symmetric and has the properties $\int W(\mathbf{r}-\mathbf{r}',h)\,\mathrm{d}\mathbf{r}' = 1$ and $\lim_{h\to 0} W(\mathbf{r}-\mathbf{r}',h) = \delta(\mathbf{r}-\mathbf{r}')$. $\sigma(\mathbf{r})$ is a measure of the particle number density which has a larger value in a dense particle region than in a dilute particle region [20]. $\chi_i(\mathbf{r})$ has the same form as the moving-least-square (MLS) approximation that reproduces the constant function, which is called Shepherd function [40]. In Flekkøy et al. [11] and Serrano and Español [37] $\chi_i(\mathbf{r})$ is employed for Voronoi-type DPD formulations. Note that $\chi_i(\mathbf{r})$ vanishes when $\mathbf{r}$ is outside of the support of $W_i(\mathbf{r})$.

The smoothing function is normalized to unity by $\sum_i \chi_i(\mathbf{r}) = 1$ and has the spatial derivatives

$$\nabla\chi_i(\mathbf{r}) = \frac{1}{\sigma(\mathbf{r})}\sum_j \left[\chi_j(\mathbf{r})\nabla W_i(\mathbf{r}) - \chi_i(\mathbf{r})\nabla W_j(\mathbf{r})\right], \tag{9}$$

where $\nabla W_i(\mathbf{r}) = \nabla W(\mathbf{r}-\mathbf{r}_i)$. We also introduce the volume of a particle through the integral over the entire domain

$$\mathscr{V}_i = \int \chi_i(\mathbf{r})\,\mathrm{d}\mathbf{r} = \int \frac{1}{\sigma(\mathbf{r})}W(\mathbf{r}-\mathbf{r}_i)\,\mathrm{d}\mathbf{r} \approx \frac{1}{\sigma_i} \tag{10}$$

which shows that $\sigma_i = \sigma(\mathbf{r}_i)$ is approximately the inverse of the particle volume, i.e., the specific volume. By the normalization property of $\chi_i(\mathbf{r})$ the partitioning condition $\sum_i \mathscr{V}_i = \mathscr{V}_{\text{total}}$ is satisfied. For a smooth variable $\psi(\mathbf{r})$ we define the particle-averaged value and the particle-averaged spatial derivative by

$$\psi_i = \frac{1}{\mathscr{V}_i}\int \chi_i(\mathbf{r})\psi(\mathbf{r})\,\mathrm{d}\mathbf{r} \quad \text{and} \quad \nabla\psi_i = \frac{1}{\mathscr{V}_i}\int \chi_i(\mathbf{r})\nabla\psi(\mathbf{r})\,\mathrm{d}\mathbf{r}, \tag{11}$$

respectively. With integration by parts and Eq. (9) the particle-averaged spatial derivative is obtained by

$$\nabla\psi_i = -\frac{1}{\mathscr{V}_i}\int \nabla\chi_i(\mathbf{r})\psi(\mathbf{r})\,\mathrm{d}\mathbf{r} = -\frac{1}{\mathscr{V}_i}\sum_j \int \frac{\psi(\mathbf{r})}{\sigma(\mathbf{r})^2}\left[W_j(\mathbf{r})\nabla W_i(\mathbf{r}) - W_i(\mathbf{r})\nabla W_j(\mathbf{r})\right]\mathrm{d}\mathbf{r}. \tag{12}$$

The right-hand side represents an inter-particle integration between particle i and j. Similarly to Eq. (10), the two integrals on the right-hand side of Eq. (12) are approximated separately to obtain

$$\nabla\psi_i \approx \sum_j \left(\frac{\psi_i}{\sigma_i^2} + \frac{\psi_j}{\sigma_j^2}\right)\sigma_i \frac{\partial W}{\partial r_{ij}}\mathbf{e}_{ij} \tag{13}$$

in which $\frac{\partial W}{\partial r_{ij}}\mathbf{e}_{ij} = \nabla W(\mathbf{r}_i - \mathbf{r}_j)$, and $\frac{\partial W}{\partial r_{ij}} \leqslant 0$, $\mathbf{r}_i - \mathbf{r}_j = \mathbf{r}_{ij} = r_{ij}\mathbf{e}_{ij}$, and $\mathbf{e}_{ij}$ is the normalized vector from particle i to j. For the particle-averaged second order spatial derivative a nested application of Eq. (13) as suggested by Flebbe et al. [10] can be used, which calculates second order derivatives from first order derivatives.

As shown in Fig. 1, the inter-particle interactions $W_i\nabla W_j$ and $W_j\nabla W_i$ vanish outside of the overlap of the supports of $W_i(\mathbf{r})$ and $W_j(\mathbf{r})$. Since all points in this domain have less distances to both particles i and j it is reasonable to substitute $\psi(\mathbf{r})$ by an inter-particle-averaged value $\overline{\psi}_{ij} = \overline{\psi}(\psi(\mathbf{r}_i), \psi(\mathbf{r}_j))$. Accordingly, the integration in Eq. (12) can be approximated as

$$\nabla\psi_i \approx -\frac{1}{\mathscr{V}_i}\sum_j \overline{\psi}_{ij}\int \frac{1}{\sigma(\mathbf{r})^2}[W_j(\mathbf{r})\nabla W_i(\mathbf{r}) - W_i(\mathbf{r})\nabla W_j(\mathbf{r})]\,\mathrm{d}\mathbf{r} \approx \sum_j \left(\frac{1}{\sigma_i^2} + \frac{1}{\sigma_j^2}\right)\sigma_i\overline{\psi}_{ij}\frac{\partial W}{\partial r_{ij}}\mathbf{e}_{ij}. \tag{14}$$

A simple inter-particle average is $\overline{\psi}_{ij} = \frac{1}{2}[\psi(\mathbf{r}_i) + \psi(\mathbf{r}_j)]$. For the particle-averaged second order spatial derivative, one can set $\psi = \nabla\varphi$, formulate the inter-particle average by $\overline{\nabla\varphi}_{ij} = \frac{\mathbf{e}_{ij}}{r_{ij}}(\varphi(\mathbf{r}_i) - \varphi(\mathbf{r}_j))$ and calculate the second-order derivative directly, which is computationally more efficient than a nested application of Eq. (13). Furthermore, Eq. (14) is more flexible because of the possibility to formulate different inter-particle averages or to assume different inter-particle distributions. For instance, Inutsuka [19] solves a Riemann problem to obtain the inter-particle average state, and as shown in Section 2.3.2, an assumed inter-particle shear stress profile is used to handle the viscosity-difference at the phase interface. Note that, by considering the effects of all particles inside the mentioned overlap domain higher-order approximations for the inter-particle integration may be derived. Therefore, Eqs. (13) and (14) may be extended to achieve higher spatial accuracy. Since the focus on this paper is on modeling of complex fluids we consider here only the straightforward approximations as stated above.

2.2. Density evolution equation

The average density of a particle is $\rho_i = m_i/\mathscr{V}_i$ in which m_i is the mass of a particle. According to Eq. (10) the evolution equation for the particle density used here is

$$\rho_i = m_i\sigma(\mathbf{r}_i) = m_i\sum_j W_{ij}, \tag{15}$$

where $W_{ij} = W(r_{ij}) = W(\mathbf{r}_i - \mathbf{r}_j)$. This form conserves mass exactly and is similar to the common SPH density approximation $\rho_i = \sum_j m_j W_{ij}$. The difference is that in the current approximation neighboring particles contribute to the particle density only by affecting the specific volume of particle i. Since there is no mass contribution from neighboring particles, Eq. (15) allows for density discontinuities when there are large particle-mass

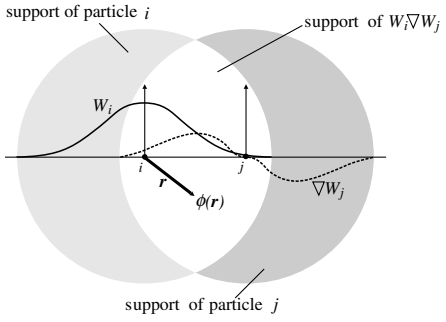

Fig. 1. Schematic for the inter-particle integration.

differences between nearby particles. Actually, if one defines the particle smoothing function as $\chi_i(\mathbf{r}) = m_i W(\mathbf{r}-\mathbf{r}_i)/\sum_k m_k W(\mathbf{r}-\mathbf{r}_k)$ as in [17] the form $\rho_i = \sum_j m_j W_{ij}$ can be derived from Eq. (10).

2.3. Momentum equation

2.3.1. Pressure

When ψ is set as the pressure p, according to Eqs. (2) and (13) the particle acceleration caused by pressure is obtained as

$$\frac{\mathrm{d}\mathbf{v}_i^{(p)}}{\mathrm{d}t} = -\frac{1}{m_i}\sum_j \left(\frac{p_i}{\sigma_i^2}+\frac{p_j}{\sigma_j^2}\right)\frac{\partial W}{\partial r_{ij}}\mathbf{e}_{ij}. \tag{16}$$

Since this expression has anti-symmetric form with respect to exchanging i and j global conservation of momentum is satisfied. Eq. (16) is similar to the form preferred by Monaghan [26]. Again, if the particle smoothing function is given by $\chi_i(\mathbf{r}) = m_i W(\mathbf{r}-\mathbf{r}_i)/\sum_k m_j W(\mathbf{r}-\mathbf{r}_k)$ the same expression can be derived with the inter-particle integral of Eq. (12).

2.3.2. Viscous force

For the flow in the bulk phase s, similar to Flekkøy et al. [11], the inter-particle-averaged shear stress is approximated as

$$\overline{\Pi_{ij}^{(v)}} = \frac{\eta^s}{r_{ij}}(\mathbf{e}_{ij}\mathbf{v}_{ij}+\mathbf{v}_{ij}\mathbf{e}_{ij}), \tag{17}$$

where $\mathbf{v}_{ij} = \mathbf{v}_i - \mathbf{v}_j$. If particle i belongs to phase k and particle j belongs to phase l one can assume that the phase interface is located at the center m between particle i and j and is normal to the inter-particle vector $\mathbf{r}_{ij}$. To ensure the continuity of shear stress and velocity across the interface one requires

$$\frac{\eta^k}{r_{im}}(\mathbf{e}_{im}\mathbf{v}_{im}+\mathbf{v}_{im}\mathbf{e}_{im}) = \frac{\eta^l}{r_{mj}}(\mathbf{e}_{mj}\mathbf{v}_{mj}+\mathbf{v}_{mj}\mathbf{e}_{mj}), \tag{18}$$

where $r_{im} = r_{mj} = \frac{1}{2}r_{ij}$, $\mathbf{e}_{im} = \mathbf{e}_{mj} = \mathbf{e}_{ij}$ and $\mathbf{v}_{ij} = \mathbf{v}_{im} + \mathbf{v}_{mj}$, as shown in Fig. 2. The inter-particle-averaged shear stress at the $k-l$ phase interface is accordingly

$$\overline{\Pi_{ij}^{(v)}} = \frac{2\eta^k\eta^l}{r_{ij}(\eta^k+\eta^l)}(\mathbf{e}_{ij}\mathbf{v}_{ij}+\mathbf{v}_{ij}\mathbf{e}_{ij}). \tag{19}$$

By comparison with Eq. (17), it can be seen that the term $\frac{2\eta^k\eta^l}{\eta^k+\eta^l}$ takes the role as a combined viscosity which has a similar form in [3,4]. Hence, the particle acceleration due to shear force at the interface in conservative form is given by

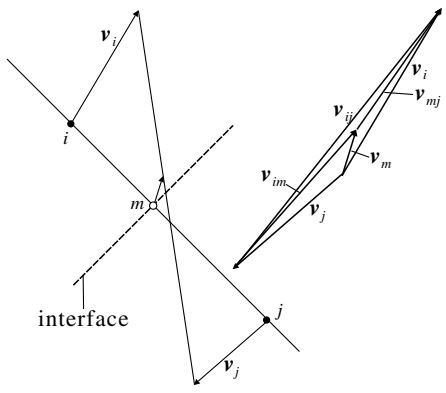

Fig. 2. Schematic for the inter-particle shear stress.

$$\frac{\mathrm{d}\mathbf{v}_i^{(v)}}{\mathrm{d}t} = \frac{1}{m_i}\sum_j \frac{2\eta^k\eta^l}{\eta^k+\eta^l}\left(\frac{1}{\sigma_i^2}+\frac{1}{\sigma_j^2}\right)\frac{1}{r_{ij}}\frac{\partial W}{\partial r_{ij}}(\mathbf{e}_{ij}\cdot\mathbf{v}_{ij}\mathbf{e}_{ij}+\mathbf{v}_{ij}). \tag{20}$$

A comparison with the viscous-force formulation in [11] shows that the term $(\frac{1}{\sigma_i^2}+\frac{1}{\sigma_j^2})\frac{\partial W}{\partial r_{ij}}\mathbf{e}_{ij}$ is equivalent to the effective inter-particle interface area. For incompressible flows, Eq. (20) simplifies to

$$\frac{\mathrm{d}\mathbf{v}_i^{(v)}}{\mathrm{d}t} = \frac{1}{m_i}\sum_j \frac{2\eta^k\eta^l}{\eta^k+\eta^l}\left(\frac{1}{\sigma_i^2}+\frac{1}{\sigma_j^2}\right)\frac{\mathbf{v}_{ij}}{r_{ij}}\frac{\partial W}{\partial r_{ij}} \tag{21}$$

according Eq. (6). Note that the expression in Eqs. (20) and (21) do not strictly conserve angular momentum. For single-phase flow an angular momentum conservative form can be derived with a nested application of Eq. (14). However, it is not clear how Eq. (14) can be applied for multi-phase flow with large viscosity difference. On the other hand, exact angular momentum conservation appears to be less important for the multi-phase flow configurations we are interested in.

2.3.3. Surface force

The computation of the interface curvature usually is cumbersome. As a remedy, in the continuous surface force model (CSF) [23], the surface force in Eq. (7) is rewritten as a tensor form $\mathbf{F}^{(1)} = \nabla\cdot\Pi^{(1)}$, where the surface stress is

$$\Pi^{(1)} = \alpha(\mathbf{I}-\hat{\mathbf{n}}\hat{\mathbf{n}})|\nabla C|. \tag{22}$$

Here, ∇C is the gradient of a color index C which has a unit jump across the interface, and $\hat{\mathbf{n}} = \frac{\nabla C}{|\nabla C|}$. Because $\mathbf{I}-\hat{\mathbf{n}}\hat{\mathbf{n}}$ has a trace of $d-1$, d is the spatial dimension, there is a negative pressure contribution $\frac{d-1}{d}\alpha|\nabla C|$ to the surface stress according to Eq. (2). As this negative pressure has no contribution to surface tension, it is reasonable to rewrite Eq. (22) as

$$\Pi^{(1)} = \alpha\left(\frac{1}{d}\mathbf{I}-\hat{\mathbf{n}}\hat{\mathbf{n}}\right)|\nabla C| \tag{23}$$

to eliminate its effects. Another reason for this procedure is that Morris [30] suggested that a negative pressure may cause stability problems in high resolution computations.

Since $|\nabla C|$ is represented numerically on an interface with finite width and approaches zero at its fringe a direct computation of $\hat{\mathbf{n}}$ may be erroneous. As suggested by Wu et al. [44] this difficulty can be resolved by rewriting Eq. (23) as

$$\Pi^{(1)} = \alpha\frac{1}{|\nabla C|}\left(\frac{1}{d}\mathbf{I}|\nabla C|^2-\nabla C\nabla C\right) \tag{24}$$

which is well defined on the entire domain and vanishes naturally when $|\nabla C|$ becomes zero.

We define the color index as

$$C_i^s = \begin{cases} 1 & \text{if particle } i \text{ belongs to } s,\\ 0 & \text{else,}\end{cases} \qquad s=1,\ldots,S \tag{25}$$

and $\sum_s C^s = 1$. The color index of each particle does not change throughout the computation. Note that the above definition is also valid for immiscible mixtures with thee or more phases. For particle i of phase k, a non-vanishing color-index gradient exists if there are neighboring particles of phase l, $l\neq k$, i.e.,

$$\nabla C_i^{kl} = \sigma_i\sum_j\left[\frac{C_i^l}{\sigma_i^2}+\frac{C_j^l}{\sigma_j^2}\right]\frac{\partial W}{\partial r_{ij}}\mathbf{e}_{ij}, \quad l\neq k \tag{26}$$

in which $C_i^l \equiv 0$. Accordingly the $k-l$ phase interface stress is obtained as

$$\Pi_{kl}^{(1)} = \alpha^{kl}\frac{1}{|\nabla C^{kl}|}\left(\frac{1}{d}\mathbf{I}|\nabla C^{kl}|^2-\nabla C^{kl}\nabla C^{kl}\right), \quad l\neq k, \tag{27}$$

where α^{kl} is surface-tension coefficient between the phases k and l. Hence, the total surface stress of particle i is

$$\Pi^{(1)} = \sum_l \Pi^{(1)}_{kl}, \quad l \neq k. \tag{28}$$

Similarly to the formulation of the pressure term the particle acceleration due to surface tension is written as

$$\frac{\mathrm{d}\mathbf{v}_i^{(1)}}{\mathrm{d}t} = \frac{1}{m_i}\sum_j \frac{\partial W}{\partial r_{ij}}\mathbf{e}_{ij}\cdot\left(\frac{\Pi_i^{(1)}}{\sigma_i^2}+\frac{\Pi_j^{(1)}}{\sigma_j^2}\right). \tag{29}$$

Note that Eq. (29) is in conservative form for both linear and angular momentum.

2.4. Mesoscopic hydrodynamics

2.4.1. Smoothed dissipative particle dynamics (SDPD)

In the current SPH method the irreversible part of the particle dynamics is

$$\begin{aligned}\dot{m}_i|_{\mathrm{irr}} &= 0,\\ \dot{\mathbf{P}}_i|_{\mathrm{irr}} &= \sum_j \frac{2\eta^k\eta^l}{\eta^k+\eta^l}\left(\frac{1}{\sigma_i^2}+\frac{1}{\sigma_j^2}\right)\frac{1}{r_{ij}}\frac{\partial W}{\partial r_{ij}}(\mathbf{e}_{ij}\cdot\mathbf{v}_{ij}\mathbf{e}_{ij}+\mathbf{v}_{ij}).\end{aligned} \tag{30}$$

According to the GENERIC formalism [14,15,38], the mass and the momentum fluctuations of particle i caused by thermal noise are postulated to be

$$\begin{aligned}\mathrm{d}\tilde{m}_i &= 0,\\ \mathrm{d}\tilde{\mathbf{P}}_i &= \sum_j B_{ij}\,\mathrm{d}\overline{\overline{\mathscr{W}}}_{ij}\cdot\mathbf{e}_{ij},\end{aligned} \tag{31}$$

where $\mathrm{d}\overline{\overline{\mathscr{W}}}_{ij}$ is the traceless symmetric part of a matrix of independent increments of a Wiener process $\mathrm{d}\mathscr{W}_{ij} = \mathrm{d}\mathscr{W}_{ji}$, i.e. $\mathrm{d}\overline{\overline{\mathscr{W}}}_{ij} = (\mathrm{d}\mathscr{W}_{ij} + \mathrm{d}\mathscr{W}_{ij}^{\mathrm{T}})/2 - \mathrm{tr}[\mathrm{d}\mathscr{W}_{ij}]\mathbf{I}/d$, d is the spatial dimension. The isothermal deterministic irreversible equations are obtained as

$$\begin{aligned}\dot{m}_i|_{\mathrm{irr}} &= 0,\\ \dot{\mathbf{P}}_i|_{\mathrm{irr}} &= -\sum_j \frac{B_{ij}^2}{4k_{\mathrm{B}}T}(\mathbf{e}_{ij}\cdot\mathbf{v}_{ij}\mathbf{e}_{ij}+\mathbf{v}_{ij})\end{aligned} \tag{32}$$

in which k_{B} is the Boltzmann constant and T is the system temperature. Comparing Eq. (32) to (30) one obtains

$$B_{ij} = \left[\frac{-8k_{\mathrm{B}}T\eta^k\eta^l}{\eta^k+\eta^l}\left(\frac{1}{\sigma_i^2}+\frac{1}{\sigma_j^2}\right)\frac{1}{r_{ij}}\frac{\partial W}{\partial r_{ij}}\right]^{1/2}. \tag{33}$$

2.4.2. Interface slip

If it is assumed that a fluid has a slightly different viscosity within a layer near the interface compared to the bulk, see Fig. 3, apparent interface slip is permitted [13]. Unlike true slip an apparent slip allows for continuous velocity and shear stress at the interface. For a $k-l$ phase particle pair the shear stress is

$$\frac{\eta^k}{r_{im}+b^{kl}}(\mathbf{e}_{im}\mathbf{v}_{im}+\mathbf{v}_{im}\mathbf{e}_{im}) = \frac{\eta^l}{r_{mj}+b^{lk}}(\mathbf{e}_{mj}\mathbf{v}_{mj}+\mathbf{v}_{mj}\mathbf{e}_{mj}), \tag{34}$$

where b^{kl} is the slip length from k phase to l phase, and from l phase to k phase it is b^{lk}. The two slip lengths are not necessarily the same. Accordingly, the inter-particle-averaged shear stress becomes

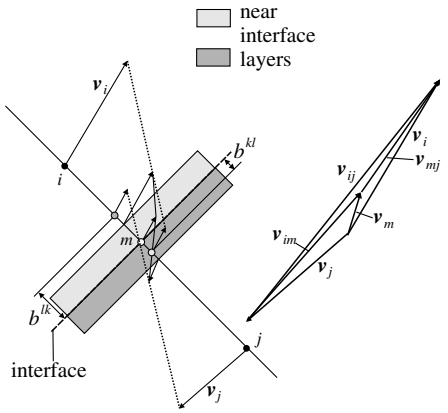

Fig. 3. Schematic for the inter-particle shear slip.

$$\overline{\Pi_{ij}^{(v)}} = \frac{2\eta^k\eta^l(\mathbf{e}_{ij}\mathbf{v}_{ij} + \mathbf{v}_{ij}\mathbf{e}_{ij})}{\eta^k(r_{ij} + 2b^{kl}) + \eta^l(r_{ij} + 2b^{lk})} \tag{35}$$

and the momentum fluctuation magnitude is

$$B_{ij} = \left[\frac{-8k_{\mathrm{B}}T\eta^k\eta^l}{\eta^k(r_{ij} + 2b^{kl}) + \eta^l(r_{ij} + 2b^{lk})}\left(\frac{1}{\sigma_i^2} + \frac{1}{\sigma_j^2}\right)\frac{\partial W}{\partial r_{ij}}\right]^{1/2}. \tag{36}$$

2.5. Solid walls

The solid body region is filled with virtual particles [34]. Whenever the support of a fluid particle overlaps with the wall surface a virtual particle is placed inside of the solid body, mirrored at the surface. The virtual particles have the same volume (i.e., mass and density), pressure and viscosity as their fluid counterparts but the velocity is given as $\mathbf{v}_{\mathrm{virtual}} = 2\mathbf{v}_{\mathrm{wall}} - \mathbf{v}_{\mathrm{real}}$ for a no-slip velocity boundary condition or $\mathbf{v}^{\tau}_{\mathrm{virtual}} = \mathbf{v}^{\tau}_{\mathrm{real}}$, where τ is the tangential direction, for a free slip boundary condition. For considering wall–fluid interactions, virtual particles are set to an independent phase w and are treated the same way as fluid particles. The corresponding fluid–wall surface energy α^{fw} and slip lengths $b^{\mathrm{wf}} = b^{\mathrm{fw}}$, if apparent slip is permitted, are also specified independently as input parameters. Currently, only straight channel walls are considered. For curved wall surfaces, the virtual particle approach may introduce considerable errors. To increase the accuracy near curved surfaces, Takada et al. [41] and Morris et al. [29] have introduced special wall particles which interact with the fluid particles in such a way that imposed boundary conditions are satisfied. How to incorporate these approaches into the current SPH formulation is one of the objectives of further investigations.

3. Numerical examples

The following two-dimensional numerical examples are provided to validate the proposed multi-phase SPH method. For all cases a quintic spline kernel [29] and a second order predictor–corrector time integration are used. A constant smoothing length, which is kept equal to the initial distance between the nearest particles, is used for all the test cases. The macroscopic results are shown in non-dimensional form, while SI units are used for mesoscopic examples to reflect the physical scales of the problems. To maintain numerical stability a Courant–Friedrichs–Lewy time step restriction based upon artificial sound speed (isothermal compressiblity), body force, viscous and surface tension is employed [26,30]. When thermal fluctuations are introduced in the mesoscopic simulation the time steps are further decreased to recover the correct kinetic temperature. Note that as there may be two or more phase interfaces with large density differences the time-step estimate based on the capillary-wave phase velocity, as suggested by Brackbill et al. [1], is modified to

$$\Delta t \leqslant 0.25 \min\left(\frac{\min(\rho_k,\rho_l)h^3}{2\pi\alpha^{kl}}\right)^{1/2}, \quad k \neq l. \tag{37}$$

Accordingly, the artificial sound speed should be comparable with

$$a^2 \sim \max\left(\frac{\alpha^{kl}\kappa_c^{kl}}{\min(\rho_k,\rho_l)\Delta}\right), \quad k \neq l, \tag{38}$$

where κ_c^{kl} is the typical curvature of the $k-l$ phase interface and Δ is the desired relative density variation.

3.1. Capillary wave

We consider two problems of circular liquid-droplet oscillation under the action of capillary forces. The first problem is a droplet oscillating in a liquid phase with the same density, i.e., $\rho_d = \rho_l$. The second problem is a droplet oscillating in a gas phase with large density ratio, i.e., $\rho_d/\rho_g \gg 1$. Numerical computations for similar problems but with different SPH implementations can be found in [30,31].

For the first problem, the computation is performed in a domain $-1/2 < x < 1/2$ and $-1/2 < y < 1/2$ using fluids of the same density $\rho_d = \rho_l = 1$ and equal viscosity $\eta = 0.05$. No-slip boundary conditions are applied at all the domain boundaries. A droplet of radius $R = 0.1875$ is placed at the domain center and the symmetry axes are $x = 0$ and $y = 0$. The surface-tension coefficient is $\alpha = 1$ and the artificial sound speed is about 10. To all particles a divergence-free initial velocity $v_x = V_0\frac{x}{r_0}(1-\frac{y^2}{r_0 r})\exp(-\frac{r}{r_0})$ and $v_y = V_0\frac{y}{r_0}(1-\frac{x^2}{r_0 r})\exp(-\frac{r}{r_0})$ is assigned, where $V_0 = 10$, $r_0 = 0.05$, and r is the distance from the position (x,y) to the droplet center. In order to study the convergence properties the calculation is carried out with 900, 3600, 14,400 particles, respectively.

Fig. 4 shows the positions of the droplet particles at $t = 0$, $t = 0.08$, $t = 0.16$ and $t = 0.26$ for a total particle number of 14,400. Comparing to the results of Morris [30] (their Fig. 6) at about the same resolution the agreement is good while our results produce a more regular particle distribution which suggests a smoother surface tension at the interface and smaller density fluctuations inside the droplet. Note that the hexagonal lattice used by Morris matches better the initial droplet geometry than our rectangle lattice. The latter, however, is easier to implement and quite suitable for symmetric shapes. Results with different resolutions are compared up to time $t = 0.5$ with 100 time samples, and the relative error between different resolutions is calculated by $E_{N,4N} = \sum_{t=0}^{0.5}|f_N - f_{4N}|$, where f_N and f_{4N} are selected global quantities. Fig. 5 compares the variation of the center-of-mass position and velocity of the upper left 1/4 part of the droplet. Convergence orders of 0.9 and 0.83, respectively, are obtained. Note there is no mass-loss error in the computations demonstrating that the current method conserves mass.

For the second problem, the initially prescribed-divergence free velocity is decreased for small amplitude oscillations. The droplet has a radius of $R = 0.2$, a density of $\rho_d = 1$, and a viscosity of $\eta_d = 5\times10^{-2}$. The gas phase has a density of $\rho_g = 10^{-3}$ and a viscosity of $\eta_g = 5\times10^{-4}$, which gives a density ratio of 1000 and a viscosity ratio of 100. The artificial sound speed is 20 or larger in order to decrease the effects of pressure waves caused by artificial compressibility. The calculation is carried out with 3600 particles in total the droplet is filled with 404 particles which is about 1/8 of that in [31]. For a free droplet oscillation, the theoretical relation between the period τ and the surface tension is $\tau = 2\pi\sqrt{\frac{R^3\rho_l}{6\alpha}}$. Fig. 6(a) shows the center-of-mass position of the upper left 1/4 part of the droplet for $\alpha = 1$. The measured period is 0.231 which is in good agreement with the theoretical value of 0.229. Note the mass center position is slightly distorted by the high frequency but low amplitude oscillations caused by artificial sound waves. The calculated relation between α and τ is plotted in Fig. 6(b) which shows that the largest deviation from the theoretical values is less than 5%.

3.2. Three-phase interaction

We consider two stationary problems with three phases. In the first problem all three phases are free to move. In the second problem a solid wall with different wetting properties is considered as a separated phase. According to the Young–Laplace theory, at equilibrium, the three phases and interfaces meet at the triple-phase point and the angles between the interfaces satisfy

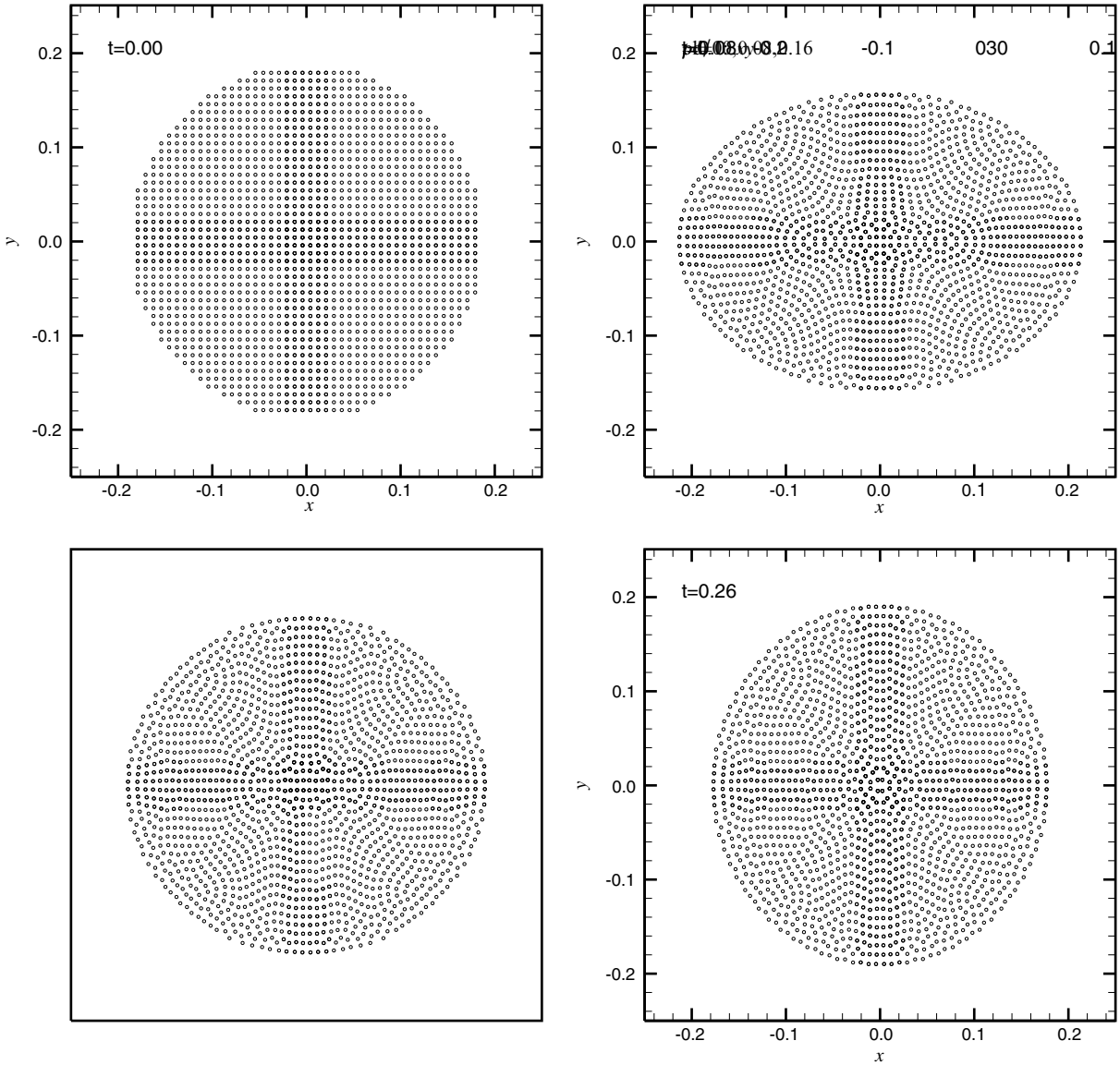

$$\begin{aligned}\alpha^{12} &= \alpha^{13}\cos\theta^{1213} + \alpha^{23}\cos\theta^{1223},\\ \alpha^{13} &= \alpha^{12}\cos\theta^{1213} + \alpha^{23}\cos\theta^{1323},\\ \alpha^{23} &= \alpha^{12}\cos\theta^{1223} + \alpha^{13}\cos\theta^{1323},\end{aligned} \tag{39}$$

where θ^{1213} stands for the angle between the 1–2 phase interface and the 1–3 phase interface, and so forth for θ^{1223} and θ^{1323}. If one of the three phases is replaced by a solid wall the respective equation in (39) simplifies to

$$\alpha^{1w} = \alpha^{12}\cos\theta + \alpha^{2w}, \tag{40}$$

where θ is the contact angle. We compare our numerical results with these analytical solution.

For the first problem the computation is performed on the domain $0 < x < 1$ and $0 < y < 0.5$ where fluid 1 occupies the top-left region, fluid 2 occupies the top-right region, and fluid 3 occupies the region defined by $y < x + 0.25$ and $y < -x + 0.75$, as shown in Fig. 7(a). Free-slip boundary conditions are applied at the

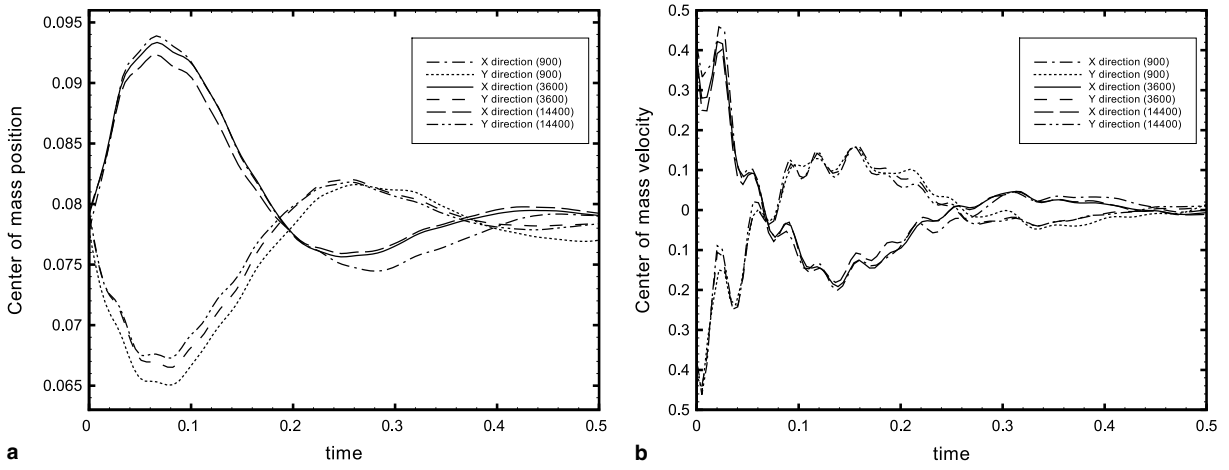

Fig. 5. Droplet oscillation with $\rho_d/\rho_l = 1$: convergence test.

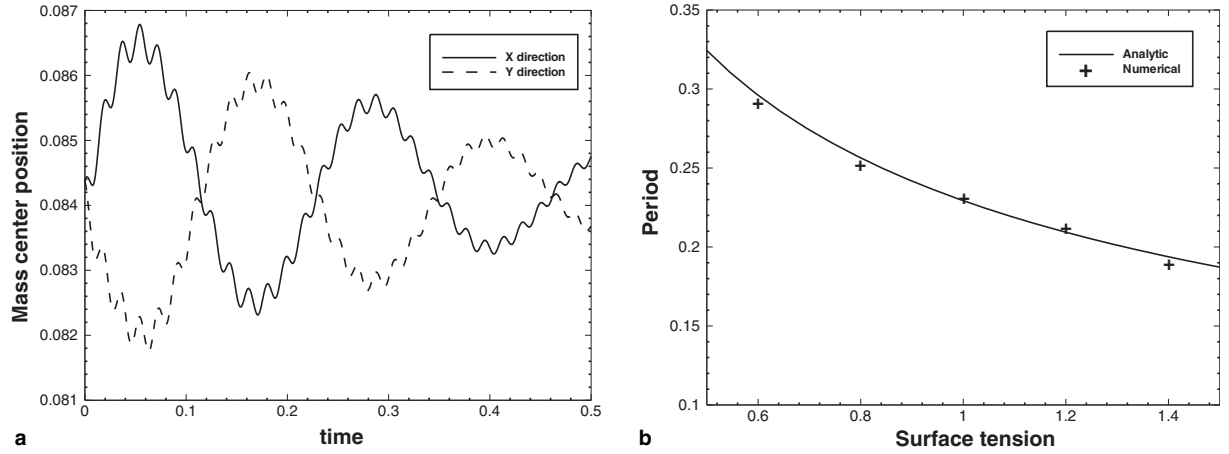

Fig. 6. Droplet oscillation with $\rho_d/\rho_g = 1000$: (a) mass center position, (b) comparison of period between the numerical and analytic results.

boundaries. The calculation is carried out with 1800 particles. Fig. 7(b) shows the positions of particles when $\alpha^{12} = \alpha^{13} = \alpha^{23} = 1$. Note the angles between all the three interfaces recover 120°, which is the analytical solution of Eq. (39). The calculations also show that, when α^{23} increases, the angle θ^{1213} decreases accordingly. Fig. 7(c) indicates the positions of particles when α^{23} is increased to 1.717. Again, the measured interface angles are in good agreement with the analytical solution which gives $\theta^{1213} = 90°$ and $\theta^{1223} = \theta^{1323} = 135°$. The consistency of the model using three different color indices for two phases is also examined. Fig. 7(d) shows the positions of particles when there is no surface tension between fluid 1 and fluid 2. The interface configuration gives $\theta^{1213} = 180°$ and $\theta^{1223} = \theta^{1323} = 90°$ which is equivalent to that of a circular interface between two phases.

For the second problem, the computation is performed on the domain $-1 < x < 1$ and $0 < y < 1$. Fluid 2 is set to occupy the region of $-0.5 < x < 0.5$ and $0 < y < 0.3$, and fluid 1 is set to occupy all the rest of the computational domain while the lower boundary is a solid wall. Free-slip boundary conditions are applied the domain boundaries and the symmetry axis is $x = 0$. The calculation is carried out with 1800 particles. For $\alpha^{12} = \alpha^{1w} = 1$ and $\alpha^{2w} = 1.5$ the measured contact angle θ is close to 120° (see Fig. 8(a)), and for $\alpha^{12} = \alpha^{1w} = 1$ and $\alpha^{2w} = 0.5$ the measured contact angle decreases to 60° (see Fig. 8(b)). Note that both results are in good agreement with the analytic solutions of Eq. (40).

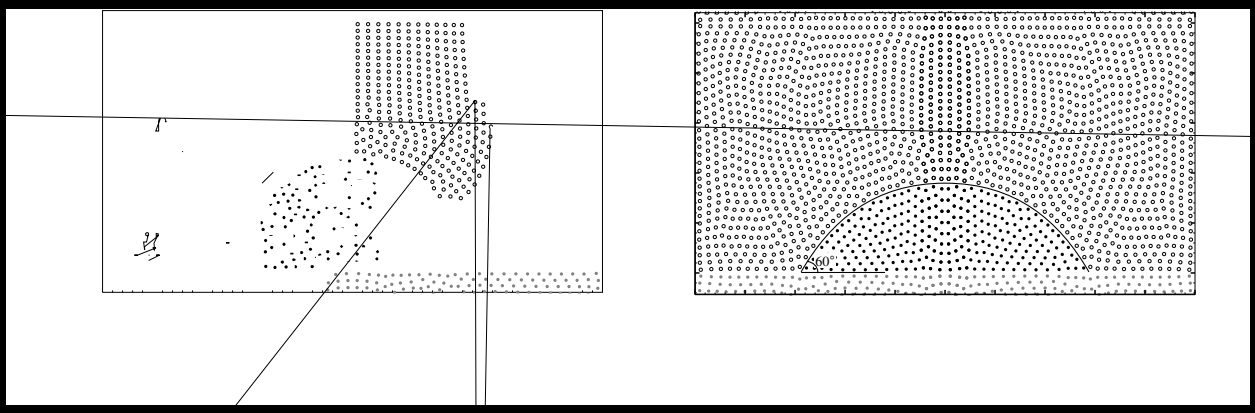
60°

B)/(

dire

With a

culated d

within 6%. N

a smaller doma

ned. Shown in F

he viscosity of the d

ingly. These results are

in a channel

three mesoscopic flow problems whi

e first problem examines the possibility

ce. The second problem evaluates the slip l

loving contact line problem. In all cases, no-s

particle placed right at the wall surface the poss

For the first problem the computational doma

carried out with 900 particles. Most of the particles

sity of 10^{-6} kg/ms while 1/3 of particles attaching

density of 25 kg/m^3 and viscosity of 2.5×10^{-7} kg/

20 nm. The top wall is assigned with the velocity c

in the flow direction. Neither surface tension nor th

problem is computed up to $t = 600$ ms, no steady

periodically while the nano-bubbles stay attached t

plotted in Fig. 11(b) which shows that there is fin

qualitative agreement with analytic work of Lauga

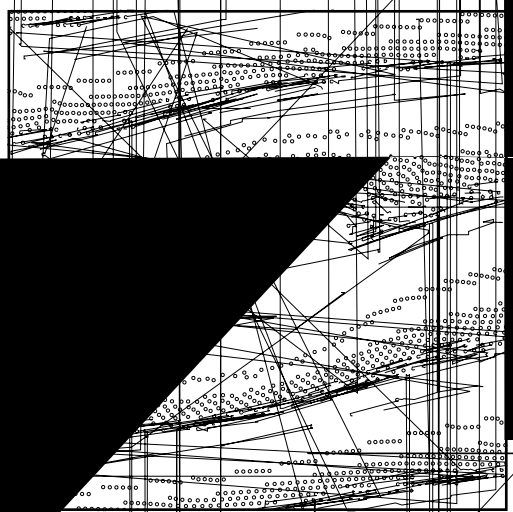

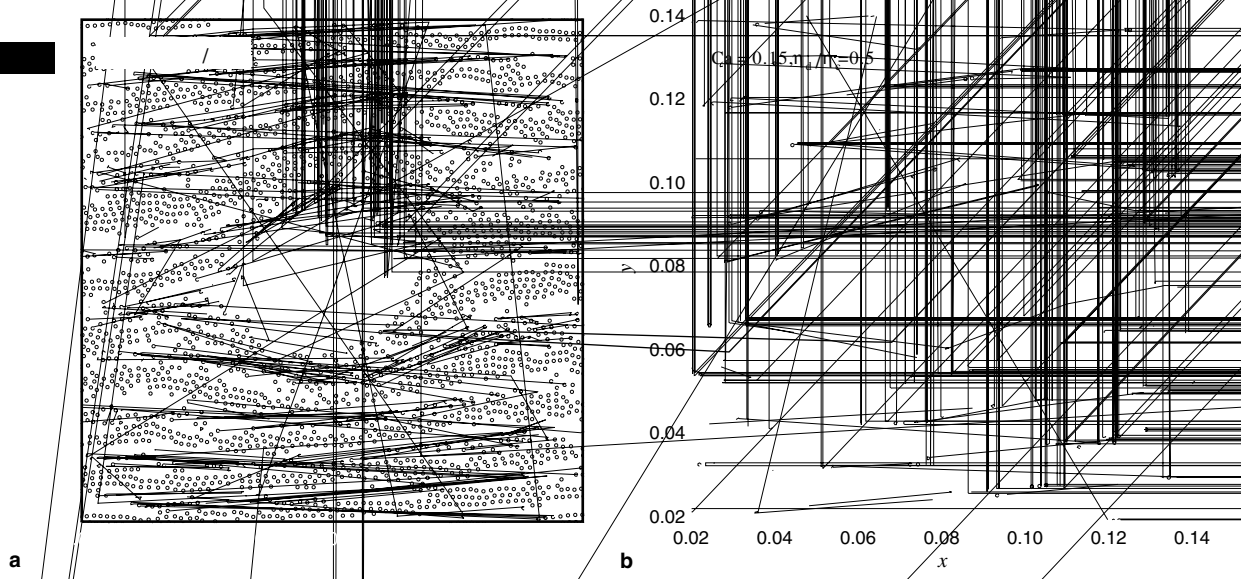

Fig. 10. Drop deformation in a shear flow: particle positions of the drop (black dots) and the shearing fluid (open circles) when $Ca = 0.2$, $Re = 0.5$, (a) $\eta_d/\eta_c = 2$ and (b) $\eta_d/\eta_c = 0.5$.

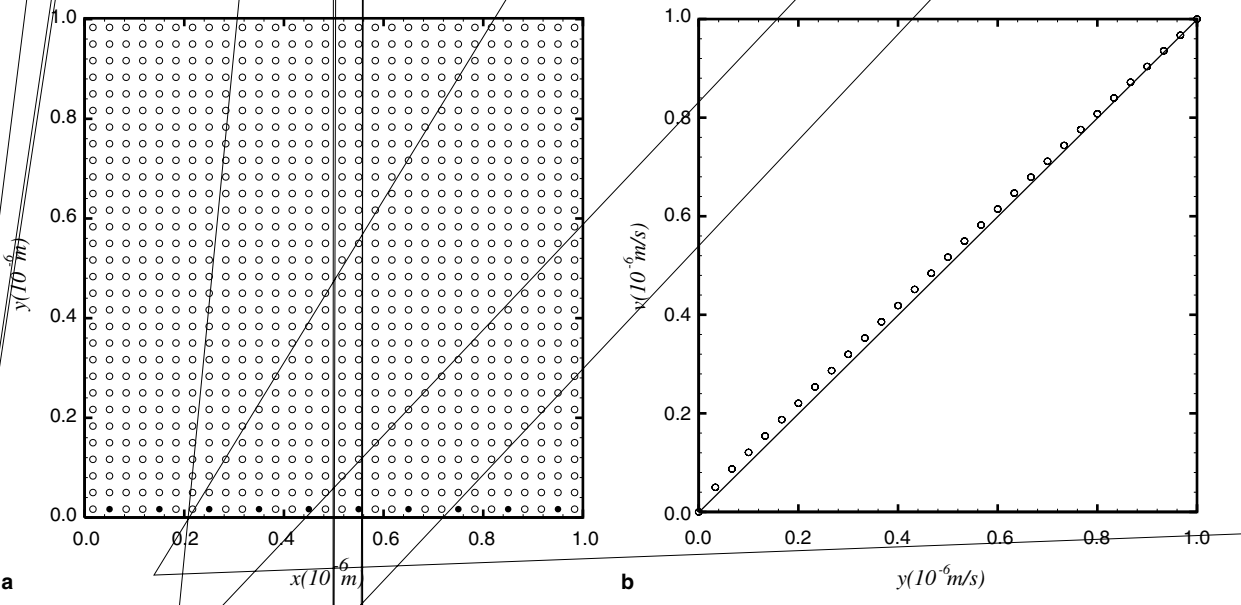

Fig. 11. Effective slip caused by nano-bubbles: (a) initial positions of the liquid (open circles) and gas (black dots) particles, (b) time-averaged velocity profile along the y direction.

by $b_e = H(v_{ave} - v)/v$ where H is the channel height, the average effective slip length is about 27 nm which has the same magnitude as is observed in several experiments [7,32].

For the second problem the same computational domain is used while the lower half is filled with fluid 1 which has the density of 1000 kg/m^3 and viscosity of 10^{-6} kg/ms, and the upper half with fluid 2 which has the same density but slightly smaller viscosity of 8×10^{-7} kg/ms. Apparent slip between the two fluids is permitted and given as $b^{12} = 50$ nm and $b^{21} = 0$. The lower wall is considered as a separate phase with an apparent slip of 50 nm at the fluid–wall surface, i.e., $b^{fw} = b^{fw} = 50$ nm. The fluid–fluid surface-tension coefficient is 10^{-9} Pa m and no surface energy is considered at the fluid–wall surface. The isothermal compressibility is given as

$a = 10^{-3}$ m/s and the thermal fluctuation is introduced with a temperature of $T = 300$ K. Periodic boundary conditions are used in the x direction. The calculation is carried out with 900 particles and time steps of about $dt = 10^{-7}$ s. To verify the thermal fluctuation the computation is first carried out without imposed shear. The calculated results show that the system reaches the correct kinetic temperature within several ms (see Fig. 12(a)). Fig. 12(b) shows the measured equilibrium momentum distribution which fits a Gaussian distribution. The equilibrium results are employed as the initial condition for further computations. The upper and lower walls are assigned with the velocity of $v = \pm 10^{-6}$ m/s, respectively. The time-averaged velocity profile along the y direction in steady state is plotted in Fig. 13(a). Note that there is considerable slip at the fluid–fluid interface and the lower fluid–wall surface. The measured slip length between the two fluids is about 24 nm and about 1/2 of b^{12}, which suggests an average effect of b^{12} and b^{21}. The measured slip velocity at the lower wall is about 4.8×10^{-6} m/s which corresponds to a slip length of 48 nm. Fig. 13(b) compares the measured and input values for several slip lengths on the wall up to 75 nm and good agreement is found.

For the third problem, we consider a mesoscopic two-phase Couette flow in a 0.5 μm × 2 μm channel. The two fluids have the same density and viscosity of 1000 kg/m^3 and 10^{-6} kg/ms, respectively. The fluid–fluid surface-tension coefficient and the two fluid–wall interface surface energy are all set as 10^{-9} Pa m and the static

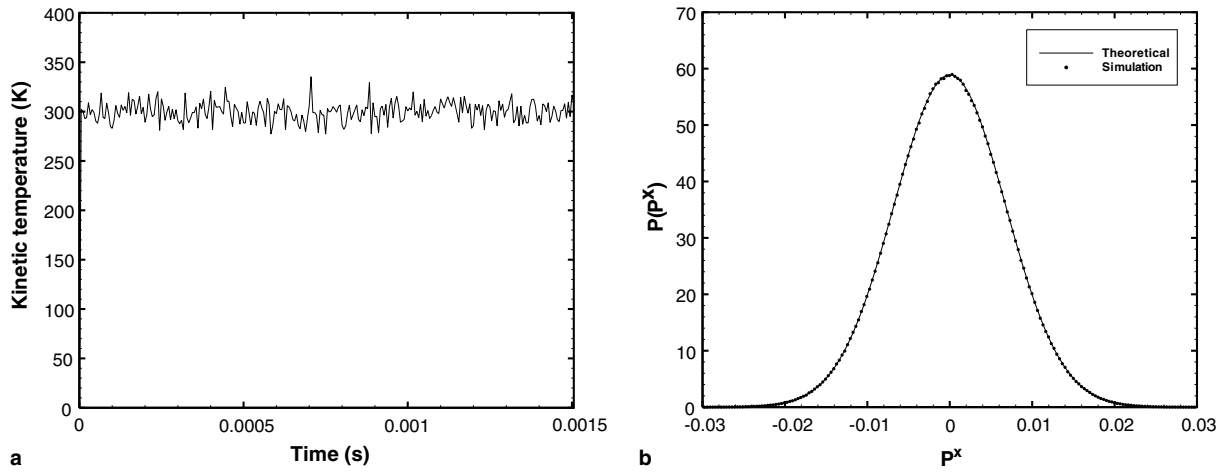

Fig. 12. Mesoscopic thermal fluctuations: (a) time evolution for kinetic temperature, (b) equilibrium momentum distribution with dimensionless unit.

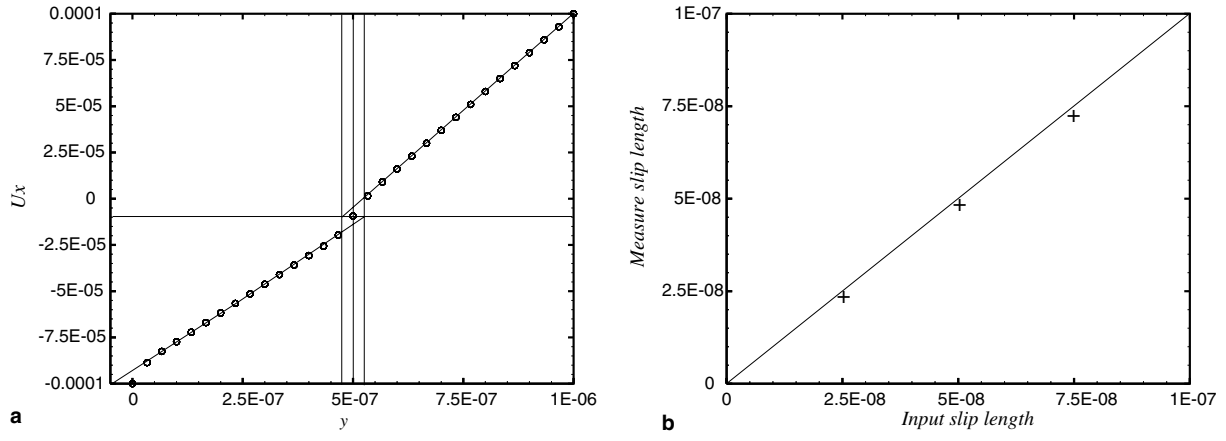

Fig. 13. Apparent slip: (a) time-averaged velocity profile (open circles) along the y direction, (b) comparison between the input slip lengths and measured values.

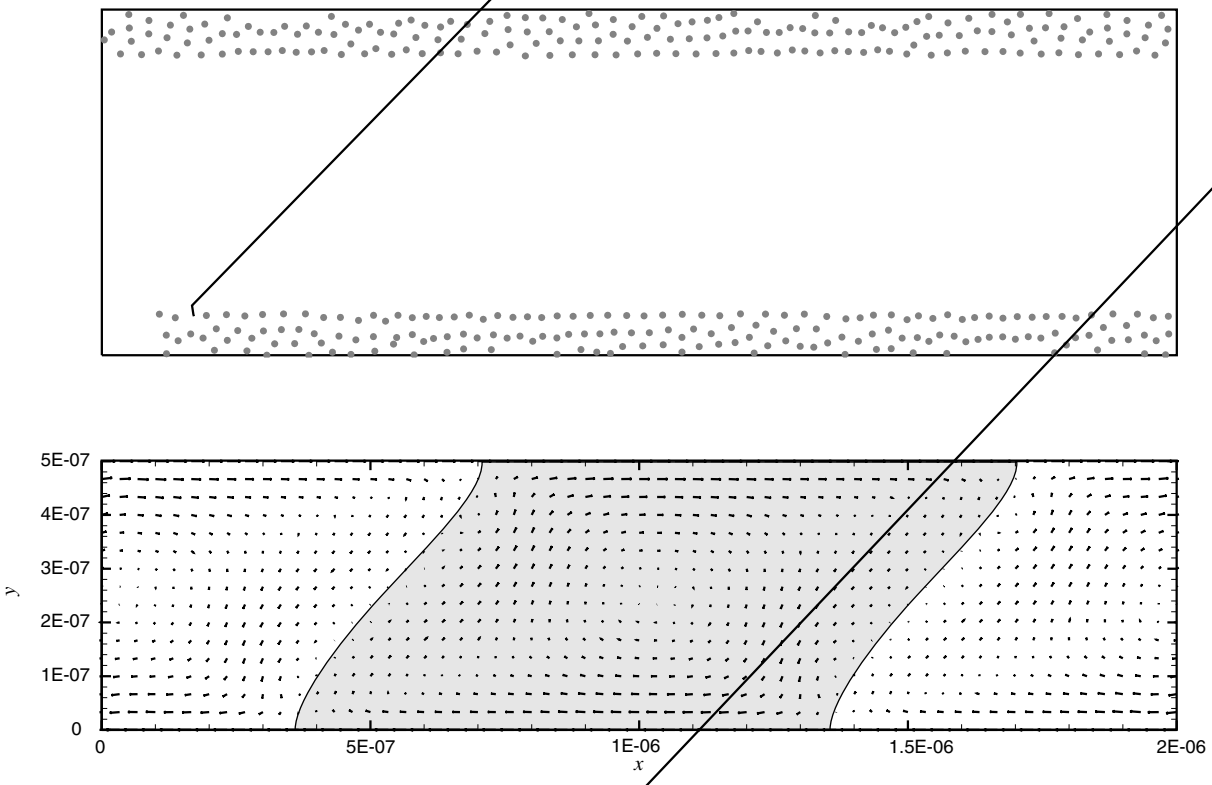

contact angle of the fluid–fluid interface at the solid wall is 90°. The upper and lower walls are assigned with velocities of $\pm 10^{-4}$ m/s, respectively . The isothermal compressibility is given as $a = 10^{-3}$ m/s and the thermal fluctuation is introduced with a temperature of $T = 300$ K. Periodic boundary conditions are used in the x direction. The calculation is carried out with 1800 particles with time steps of about $\mathrm{d}t = 10^{-7}$ s. Fig. 14 shows the instantaneous particle positions for the steady state and the time-averaged velocity field and interface position. Note that for regions far from the contact line the velocity profile along the y direction is typical for Couette flow while large deviations exist in the regions near the contact line (see Fig. 14). These results are in qualitative agreement with MD simulations of Thompson and Robbins [43] and Qian et al. [33]. Note that the current results are obtained with no-slip boundary conditions which suggest that the slip near the contact line actually is an apparent slip and there is no real slip right at the wall surface.

4. Concluding remarks

We have developed a multi-phase SPH method from a particle smoothing function in which the neighboring particles only contribute to the specific volume but not density. While handling density discontinuity naturally and conservatively the new method is also capable of multi-viscosity, multi-surface tension, fluid–wall interactions, mesoscopic thermal fluctuations, and interface slippage. Numerical examples are investigated and compared with analytic solutions, previous results and experiments. The results suggest that the method can be faithfully applied to both macroscopic and mesoscopic multi-phase flows. Since its construction is based on the standard SPH method the involved approximations are simple to implement and suitable for straightforward extension to three dimensions. In addition, since the color index of each particle does not change throughout the computation and, therefore, no color-index evolution equation is needed, the computational cost only increases slightly when the number of phases is increased. Finally, as the currently used inter-particle integration approximation for determining the particle-averaged spatial derivatives can be extended to more

accurate formulations our method suggests a way for implementing SPH methods with higher order of accuracy.

References

[1] J.U. Brackbill, D.B. Kothe, C. Zemach, A continuum method for modeling surface tension, J. Comput. Phys 100 (1992) 335.
[2] S. Chen, G.D. Doolen, Lattice Boltzmann method for fluid flows, Annu. Rev. Fluid Mech. 30 (1998) 329.
[3] P. Cleary, Modelling confined multi-material heat and mass flows using SPH, Appl. Math. Modelling 22 (1998) 981.
[4] P. Cleary, J. Ha, V. Alguine, T. Nguyen, Flow modelling in casting processes, Appl. Math. Modelling 26 (2002) 171.
[5] A. Colagrossi, M. Landrini, Numerical simulation of interfacial flows by smoothed particle hydrodynamics, J. Comput. Phys. 191 (2003) 448.
[6] G.H. Cottet, P. Koumoutsakos, Vortex Methods: Theory and Practice, Cambridge University Press, Cambridge, 2000.
[7] C. Cottin-Bizonne, S.J. Jurine, J. Baudry, J. Crassous, F. Restagno, E. Charlaix, Nanorheology: an investigation of the boundary condition at hydrophobic and hydrophilic interfaces, Eur. Phys. J. E 9 (2002) 47.
[8] P. Español, P. Warren, Statistical mechanics of dissipative particle dynamics, Europhys. Lett. 30 (1995) 191.
[9] P. Español, M. Revenga, Smoothed dissipative particle dynamics, Phys. Rev. E 67 (2003) 026705.
[10] O. Flebbe, S. Munzel, H. Herold, H. Ruder, Smoothed particle hydrodynamics: physical viscosity and the simulation of accretion disks, Astrophys. J. 431 (1994) 754.
[11] E.G. Flekkøy, P.V. Coveney, G. de Fabritiis, Foundations of dissipative particle dynamics, Phys. Rev. 62 (2000) 2140.
[12] R.A. Gingold, J.J. Monaghan, Smoothed particle hydrodynamics – Theory and application to non-spherical stars, Mon. Not. R. Astron. Soc 181 (1977) 375.
[13] S. Granick, Y. Zhu, H. Lee, Slippery questions about complex fluids flowing past solids, Nat. Mater. 2 (2003) 221.
[14] M. Grmela, H.C. Öttinger, Dynamics and thermodynamics of complex fluids, I. Development of a general formalism, Phys. Rev. E 56 (1997) 6620.
[15] H.C. Öttinger, M. Grmela, Dynamics and thermodynamics of complex fluids, II. Illustrations of a general formalism, Phys. Rev. E 56 (1997) 6633.
[16] R.D. Groot, P.B. Warren, Dissipative particle dynamics: bridging the gap between atomistic and mesoscopic simulation, J. Chem. Phys. 107 (1997) 4423.
[17] D. Hietel, K. Steiner, J. Struckmeier, A finite-volume particle method for compressible flows, Math. Models Meth. Appl. Sci. 10 (2000) 1363.
[18] P.J. Hoogerbrugge, J. Koelman, Simulating microscopic hydrodynamic phenomena with dissipative particle dynamics, Europhys. Lett. 19 (1992) 155.
[19] S. Inutsuka, Reformulation of smoothed particle hydrodynamics with Riemann solver, J. Comput. Phys. 179 (2002) 238.
[20] S. Koshizuka, A. Nobe, Y. Oka, Numerical analysis of breaking waves using the moving particle semi-implicit method, Int. J. Numer. Meth. Fluids 26 (1998) 751.
[21] J. Koplik, J.R. Banavar, Continuum deductions from molecular hydrodynamics, Annu. Rev. Fluid Mech. 27 (1995) 257.
[22] P. Koumoutsakos, Multiscale flow simulations using particles, Annu. Rev. Fluid Mech. 37 (2005) 457.
[23] B. Lafaurie, C. Nardone, R. Scardovelli, S. Zaleski, G. Zanetti, Modelling merging and fragmentation in multiphase flows with SURFER, J. Comput. Phys. 113 (1994) 134.
[24] E. Lauga, H.A. Stone, Effective slip in pressure-driven Stokes flow, J. Fluid Mech. 489 (2003) 55.
[25] L.B. Lucy, A numerical approach to the testing of the fission hypothesis, Astron. J. 82 (1977) 1013.
[26] J.J. Monaghan, Smoothed particle hydrodynamics, Annu. Rev. Astronom. Astrophys. 30 (1992) 543.
[27] J.J. Monaghan, Simulating free surface flows with SPH, J. Comput. Phys. 110 (1994) 399.
[28] J.J. Monaghan, A. Kocharyan, SPH simulation of multi-phase flow, Comput. Phys. Commun. 87 (1995) 225.
[29] J.P. Morris, P.J. Fox, Y. Zhu, Modeling low Reynolds number incompressible flows using SPH, J. Comput. Phys. 136 (1997) 214.
[30] J.P. Morris, Simulating surface tension with smoothed particle hydrodynamics, Int. J. Numer. Meth. Fluids 33 (1999) 333.
[31] S. Nugent, H.A. Posch, Liquid drops and surface tension with smoothed particle applied mechanics, Phys. Rev. E 62 (2000) 4968.
[32] R. Pit, H. Hervet, L. Leger, Direct experimental evidence of slip in hexadecane: solid interfaces, Phys. Rev. Lett. 85 (2000) 980.
[33] T. Qian, X.P. Wang, P. Sheng, Molecular scale contact line hydrodynamics of immiscible flows, Phys. Rev. E 68 (2003) 016306.
[34] P.W. Randles, L.D. Libersky, Smoothed particle hydrodynamics: some recent improvements and applications, Meth. Appl. Mech. Eng. 139 (1996) 375.
[35] B.W. Richie, P.A. Thomas, Multiphase smoothed-particle hydrodynamics, Mon. Not. R. Astron. Soc 323 (2001) 743.
[36] R. Scardovelli, S. Zaleski, Direct numerical simulation of free-surface and interfacial flow calculations, Annu. Rev. Fluid Mech. 31 (1999) 567.
[37] M. Serrano, P. Español, Thermodynamically consistent mesoscopic fluid particle model, Phys. Rev. E 64 (2001) 046115.
[38] M. Serrano, G. de Fabritiis, P. Español, E. Flekkoy, P.V. Coveney, Mesoscopic dynamics of Voronoi fluid particles, J. Phys. A 35 (2002) 1605.
[39] J.A. Sethian, P. Smereka, Level-set methods for fluid interfaces, Annu. Rev. Fluid Mech. 35 (2003) 341.
[40] D. Shepherd, A two dimensional function for irregularly space data, in: ACM National Conference, 1968.
[41] H. Takeda, S.M. Miyama, M. Sekiya, Numerical simulation of viscous flow by smoothed particle hydrodynamics, Prog. Theor. Phys. 92 (1994) 939.

[42] G.I. Taylor, The formation of emulsions in de.nable.elds of flows, Proc. R. Soc. Lond. A 146 (1934) 501.
[43] P.A. Thompson, M.O. Robbins, Simulations of contact-line motion: slip and the dynamic contact angle, Phys. Rev. Lett. 63 (1989) 766.
[44] J. Wu, S.T. Yu, B.N. Jiang, Simulation of two-fluid flows by the least-square finite element method using a continuum surface tension model, Int. J. Numer. Meth. Eng. 42 (1998) 583.
[45] H. Zhou, C. Pozrikidis, The flow of suspensions in channels: single files of drops, Phys. Fluids A 5 (1993) 311.